



Supplementary Information for

The role of ENSO in modulating hydroxyl: feedbacks and variability in the absence of external forcing

Alexander J. Turner, Inez Fung, Vaishali Naik, Larry W. Horowitz, and Ronald C. Cohen

Alexander J. Turner.
E-mail: alexjturner@berkeley.edu

This PDF file includes:

Supplementary text
Figs. S1 to S10
References for SI reference citations

Supporting Information Text

Introduction. This supporting information contains three sections of text and ten additional figures. Text S1 discusses the impact of computer architecture on the OH anomalies. Text S2 discusses the robustness of the EOFs. Text S3 discusses the robustness of simple OH parameterizations using short atmospheric records. Figure S1 shows the impact of including the boundary layer in the wavelet analysis. Figure S2 shows the impact of changing computer architecture on the OH anomalies. Figure S3 shows a wavelet analysis of the NINO3.4 SST anomalies. Figure S4 shows the second EOF and corresponding principal component. Figure S5 shows the distribution of correlations between EOFs from sub-sampled 100-year records and the full 3000-year record. Figure S6 shows the percent of variance explained by the different EOF patterns for the full 3000-year record and the sub-sampled 100-year records. Figure S7 shows the correlations between OH and its driving factors as a function of record length. Figure S8 shows the leading principal component from main text Fig. 4 but includes the lightning NO_x emission anomalies. Figure S9 shows the HadISST1 SSTs in the Tropical Pacific from 1980-2017. Figure S10 is the same as main text Fig. 3 but for the methane lifetime ($k(T) \times [\text{OH}]$).

Text S1. Impact of computer architecture on the OH anomalies

We only use years 3000-6000 from the preindustrial control simulation in the analysis presented in this manuscript. This is because we find a $\sim 3\text{-}5\%$ shift in the global mean OH anomalies in the year 1070 (see Fig. S2). This coincides with a change in computer architecture. The preindustrial control simulation was run over a ~ 6 year period:

- **years 1-879:** ran on the GFDL SGI Altix machine from 2009-2010
- **years 880-1070:** ran on the NASA SGI Altix machine from 2011-2012
- **years 1071-6600:** ran on the ORNL Cray machines from 2012-2016

The bottom left panel of Fig. S2 shows the OH anomalies for these three periods and the right panel shows the distribution of OH anomalies. The change in architecture (from SGI Altix machines to Crays) resulted in a slight shift in the equilibrium state. As such, our analysis focused on years 3000-6000 to allow for a long spinup and a consistent computer architecture.

Text S2. Robustness of the EOFs.

Figure S4 shows the second EOF and PC of the OH anomalies from main text Fig. 3. This second EOF pattern is a largely positive anomaly in the Tropics centered over the Atlantic Ocean. Given the importance of the tropics in the production of OH, it's not surprising that this general feature stands out as this region accounts for much of the OH production. However, it is unclear if this EOF is a robust signal. Figure S5 shows the distribution of correlations between the EOFs computed using the full 3000-year record and 100-year records with a randomly sampled initial year. If the EOF pattern is robust then we would expect the EOF computed with the 100-year record to be strongly correlated with the EOF from the full 3000-year record. The distribution of correlations for EOF 1 indicates that the first EOF is a robust feature (blue histogram in Fig. S5). In contrast, the distribution of correlations for EOF 3 peaks around ~ 0.1 indicating that EOFs 3+ are not a robust pattern of variability. It is unclear if EOF 2 is a robust feature; the distribution of correlations for EOF 2 peaks at ~ 0.5 but is skewed towards low correlations. Figure S6 shows the variance explained by the EOFs for the full 3000-year record (dashed blue line) and for the sub-sampled 100-year records (black line and gray shading). We find that EOF 1 explains 17% of the variance in the full 3000-year record but explains $25 \pm 3\%$ of the variance in the 100-year records. This indicates that ENSO is the dominant pattern of variability in both the full 3000-year record and for shorter 100-year records. It also implies that ENSO explains more of the variability on decadal-to-centennial timescales, relative to millennial timescales.

Text S3. Deriving simple OH parameterizations based on short atmospheric records.

Previous work has developed simple parameterizations of OH or the methane lifetime due to reaction with OH ($\tau_{\text{CH}_4 \times \text{OH}}$). For example, Holmes *et al.*(1) used 10 years of data to develop a five parameter model for $\tau_{\text{CH}_4 \times \text{OH}}$: temperature, water vapor, column ozone, lightning NO_x emissions, and biomass burning emissions. This is appealing because it would allow us to obtain an estimate of OH without performing computationally expensive model simulations and may help project future OH burdens. We use the long-record from our 3000-year control run to investigate how long of a record we need to robustly derive such a relationship. Fig. S7 shows the distribution of correlations between OH, lightning NO_x , water vapor, $J(\text{O}^1\text{D})$, and temperature. We find that the $1\text{-}\sigma$ spread in correlations between OH anomalies and its potential drivers is ~ 0.5 . In many cases we could derive either positive or negative relationships over a 10-year period with OH and these driving factors. Using 10 years, only lightning NO_x emissions robustly return a correlation of the same sign. From this we conclude that using short atmospheric records (< 100 years) could lead to erroneous relationships between OH and its potential drivers.

Wavelet power spectrum (deseasonalized 23°N–23°S OH anomalies)

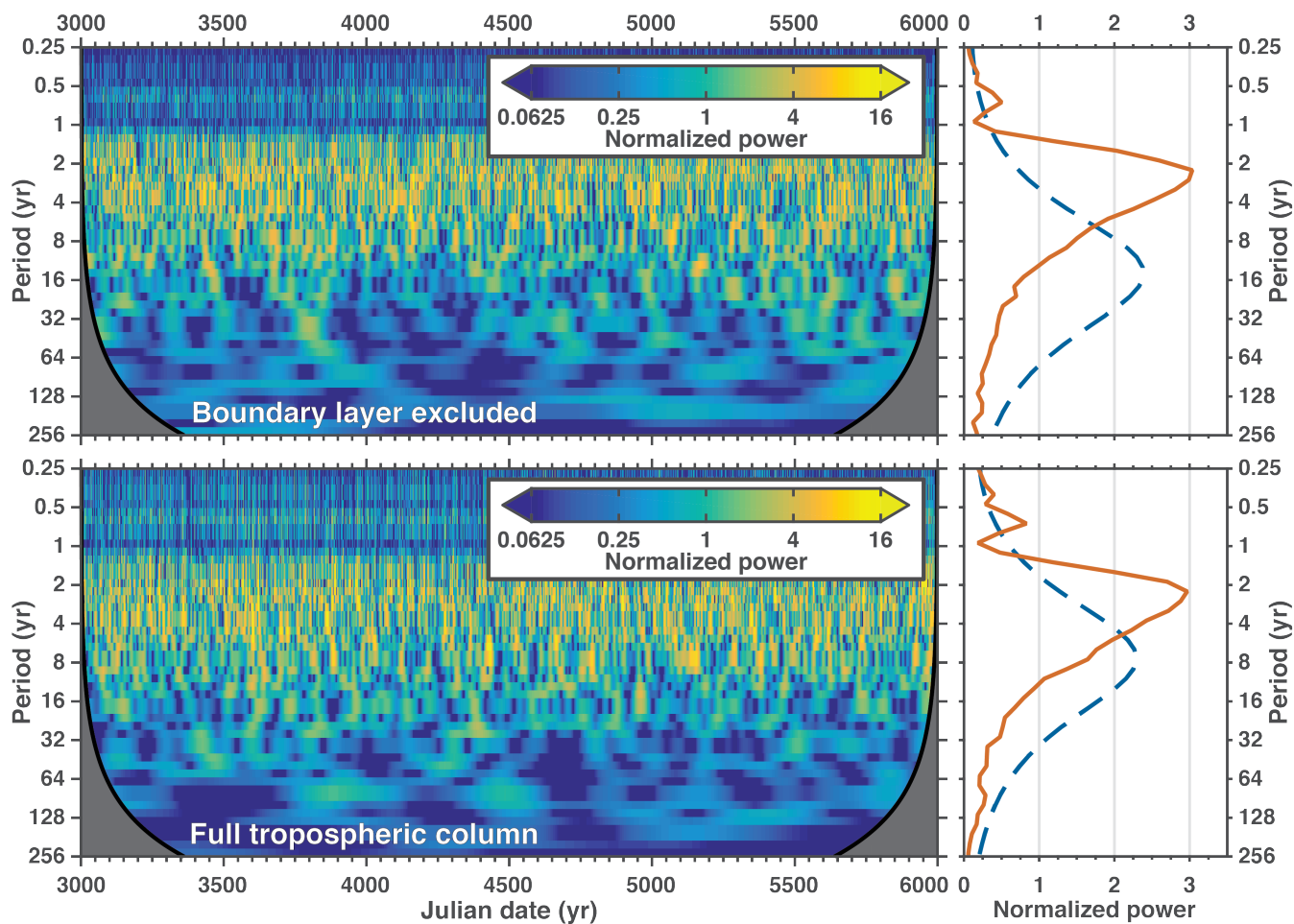


Fig. S1. Wavelet analysis examining the impact of including the boundary layer. Main text analysis excluded the boundary layer because GHG concentrations were prescribed below 800 hPa. Left column is the bias-rectified local wavelet power spectrum using a Morlet wavelet. Right column is the global wavelet spectrum (solid red line) and the 95% confidence level (dashed blue line). Top row is using the free-tropospheric OH anomalies and the bottom row is using the full tropospheric column. Anomalies have been normalized to unit variance to facilitate comparison.

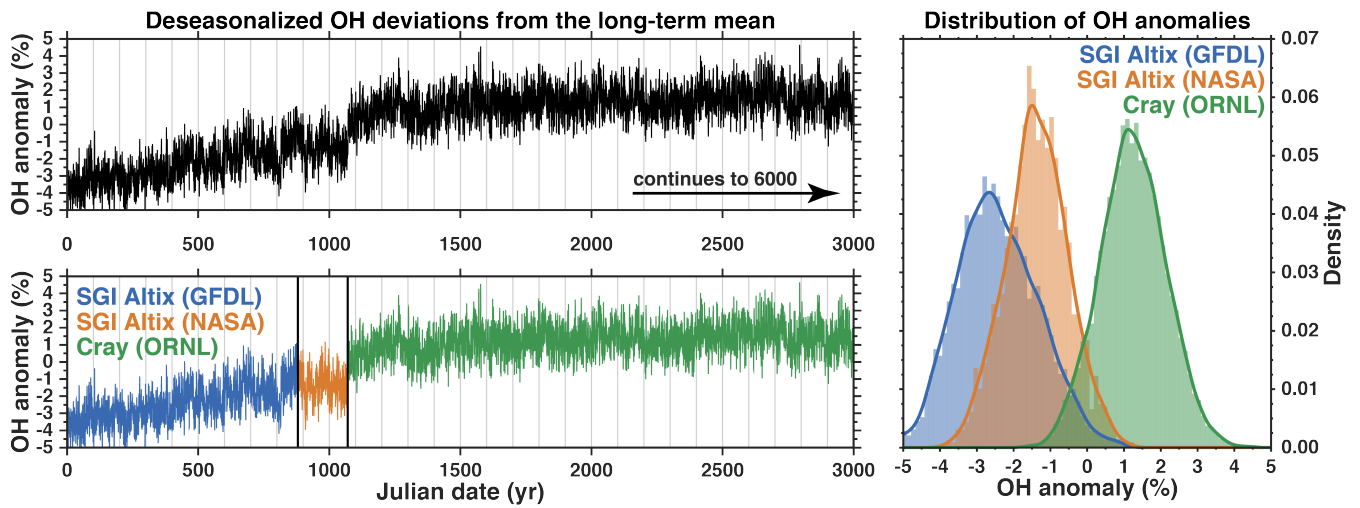


Fig. S2. OH anomalies in a control simulation. Top left panel shows the monthly OH anomalies in the troposphere (pressure weighted) from 0-3000 yr in the GFDL CM3 control run. OH anomalies are the deseasonalized OH deviations from the long-term mean, normalized to the long-term mean, and expressed as a percentage: $(x - \bar{x}) \cdot \bar{x}^{-1}$. Seasonal cycle is removed using a stable seasonal filter. Bottom left panel is the same as the top right but colored based on the computing system used. Right panel shows the distribution of OH anomalies (colored bars) for the control simulation on the three computing architectures.

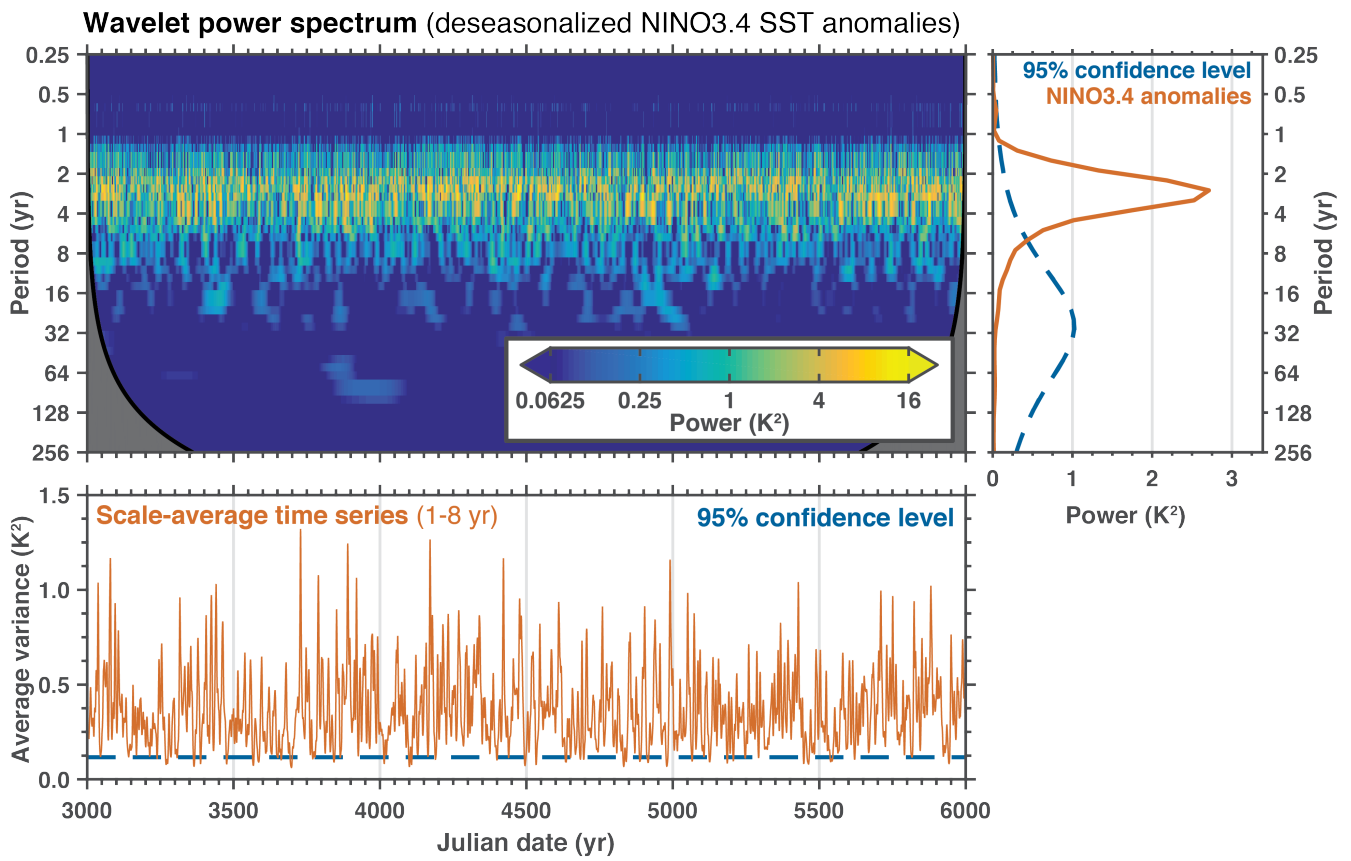


Fig. S3. Wavelet analysis of the NINO3.4 SST anomalies. Same as main text Fig. 2 but for the NINO3.4 SST anomalies. NINO3.4 region is defined as 5°N–5°S, 120°–170°W.

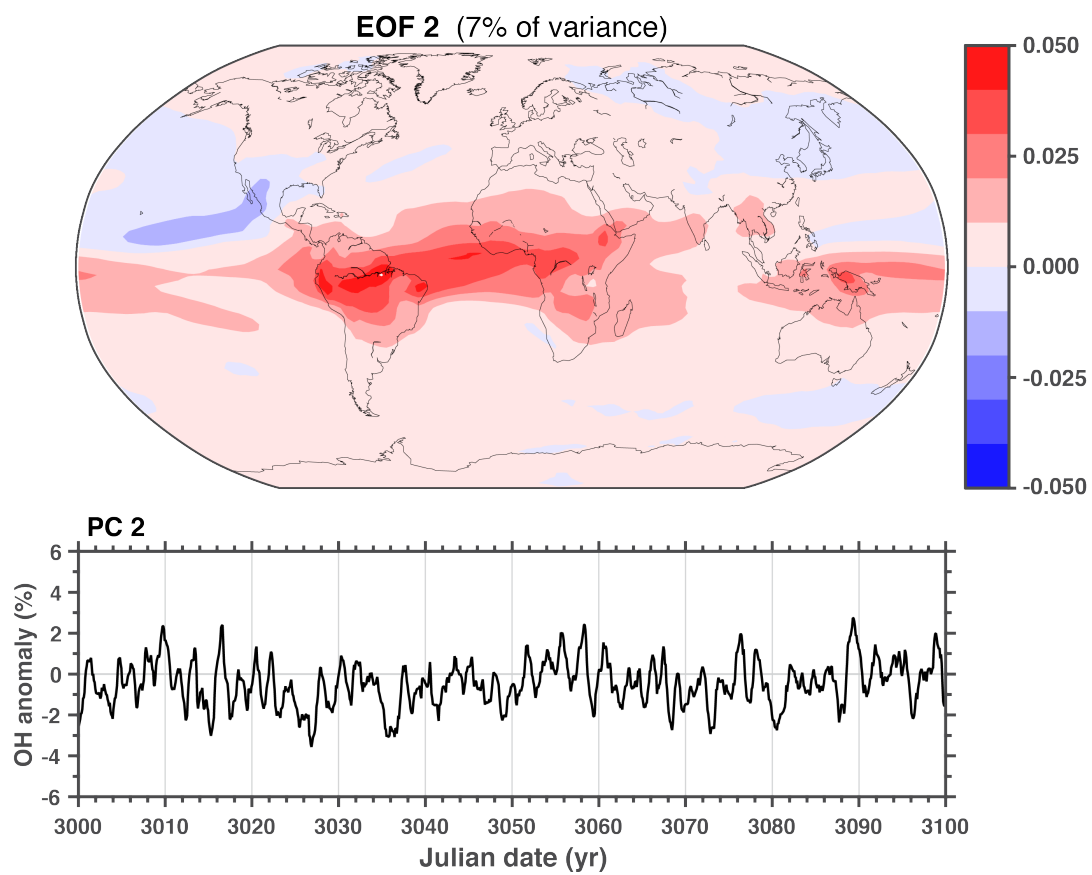


Fig. S4. EOF 2 and the associated principal component. Same as right column from main text Fig. 3 except for EOF 2 and PC 2.

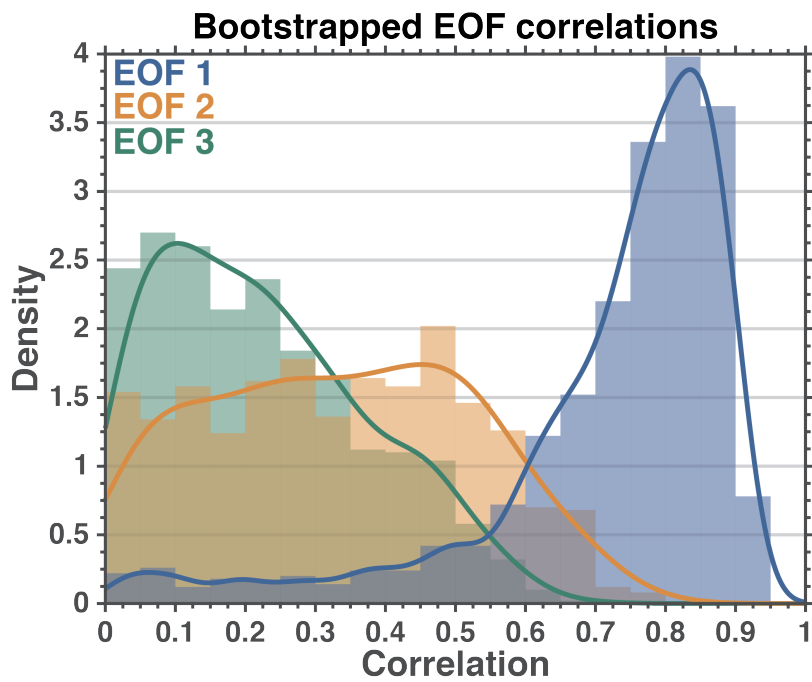


Fig. S5. Distribution of correlations between EOFs from 100-year records and the full 3000-year record. We randomly sampled 100-year records from the full 3000-year record and computed the EOFs for the shorter record. Distribution shows the correlation between the short record and the full record for EOF 1 (blue), EOF 2 (orange), and EOF 3 (green).

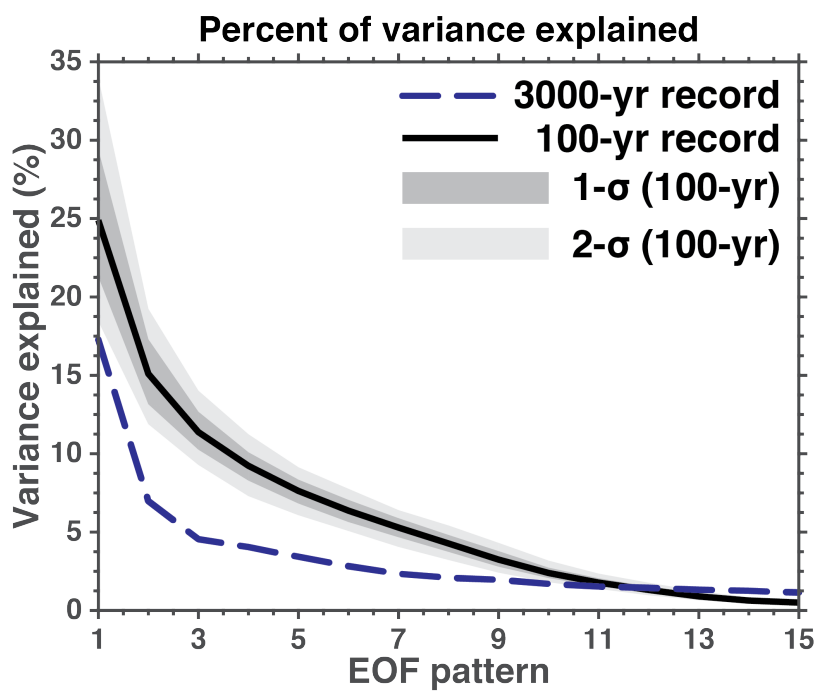


Fig. S6. Percent of variance explained. The variance explained by each EOF pattern for the full 3000-year record (dashed blue line). The median variance explained for a random sampling of 100-year records (solid black line) and uncertainty (gray shading) is also shown. Random sampling is the same as Fig S5.

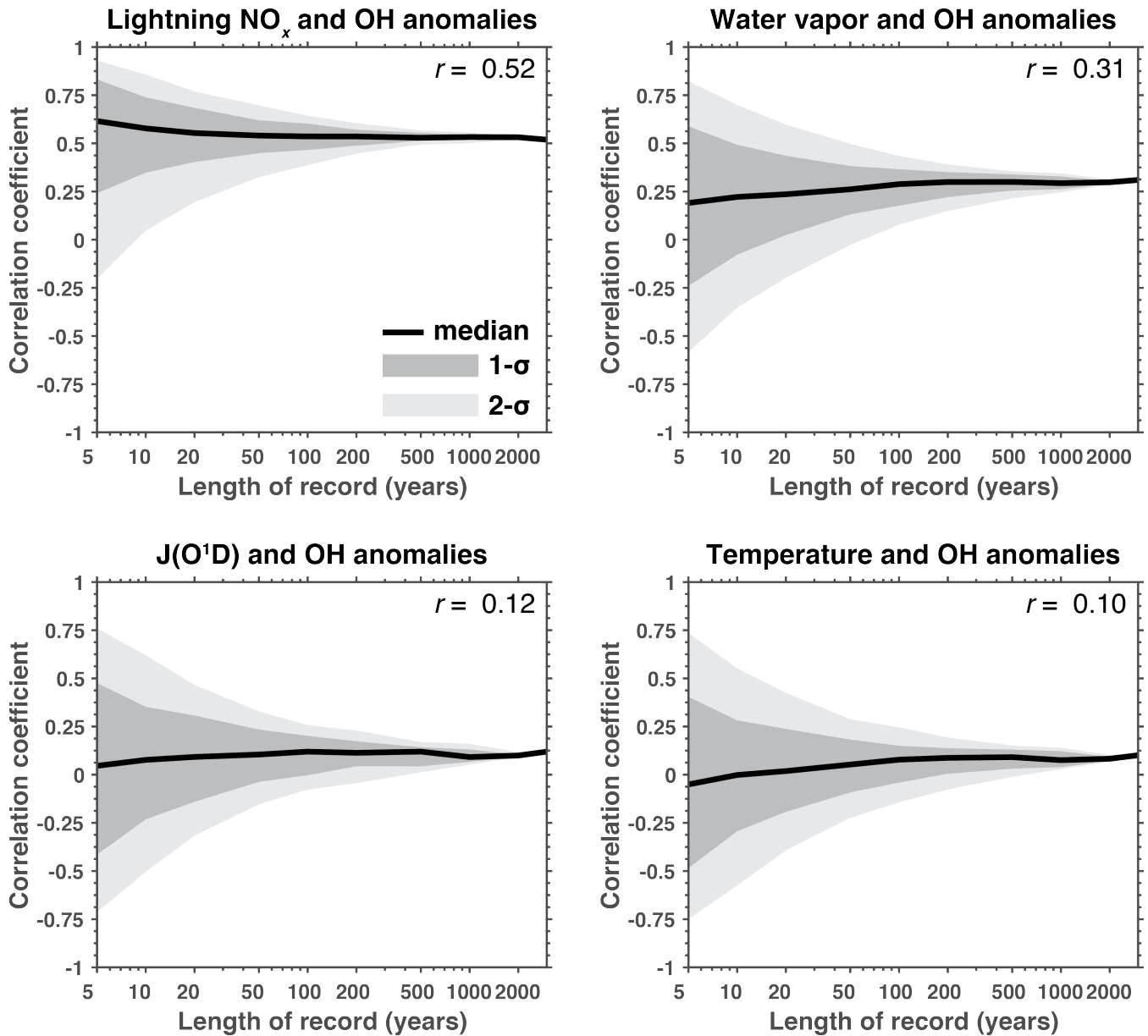


Fig. S7. Correlations between OH and its driving factors. We randomly draw different records from the full 3000-year record and compute the correlation between OH and its potential drivers. x-axis denotes the record length used in the correlation. Correlation coefficient listed is the using the full 3000-year record. Top left panel shows Lightning NO_x emission anomalies, top right panel shows water vapor (specific humidity) anomalies, bottom left shows J(O¹D) anomalies, and bottom right shows temperature anomalies. All quantities have been deseasonalized in the same manner as the OH anomalies.

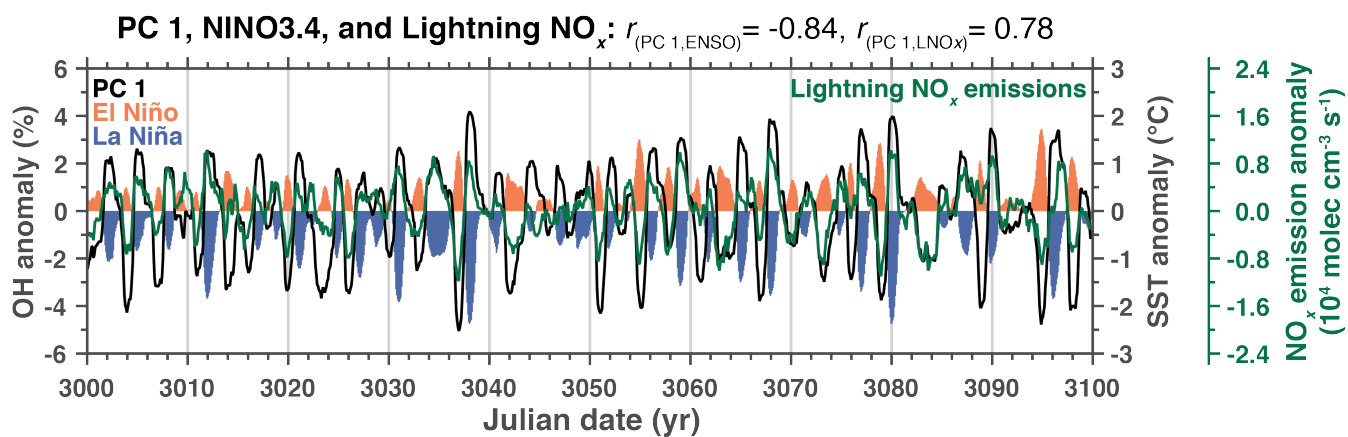


Fig. S8. PC 1 including lightning NO_x emissions. Same as main text Fig. 3d but including lightning NO_x emission anomalies (green line).

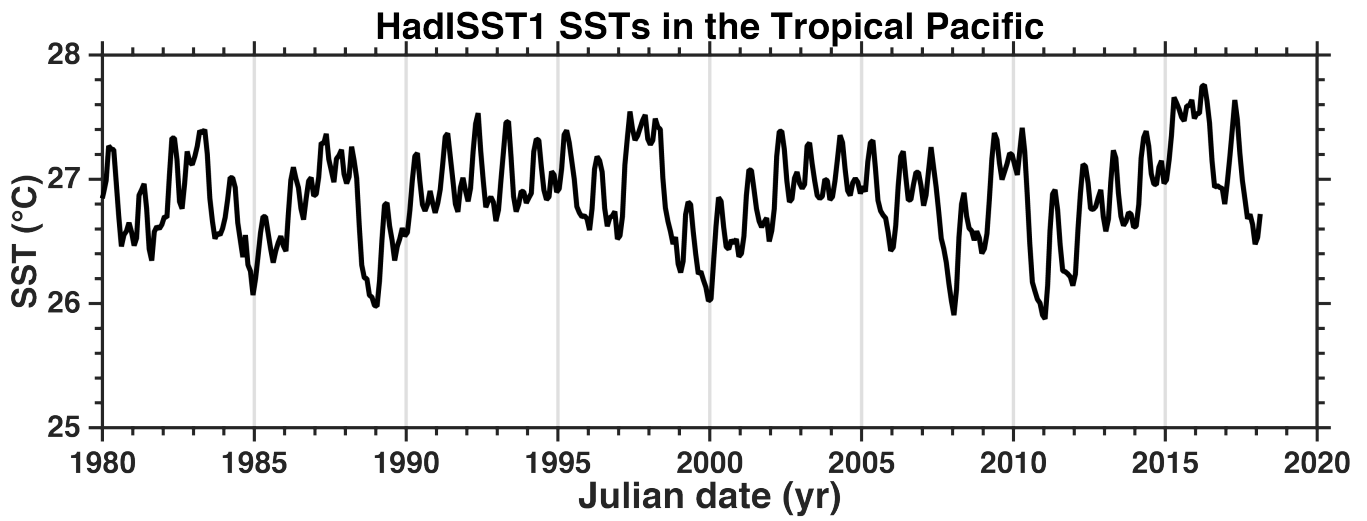


Fig. S9. Tropical Pacific SSTs from 1980-2017. 1980-2017 monthly mean sea surface temperatures (SSTs) in the Tropical Pacific (23°N–23°S; 160°E–90°W) from HadISST1 (<https://www.metoffice.gov.uk/hadobs/hadisst/data/download.html>).

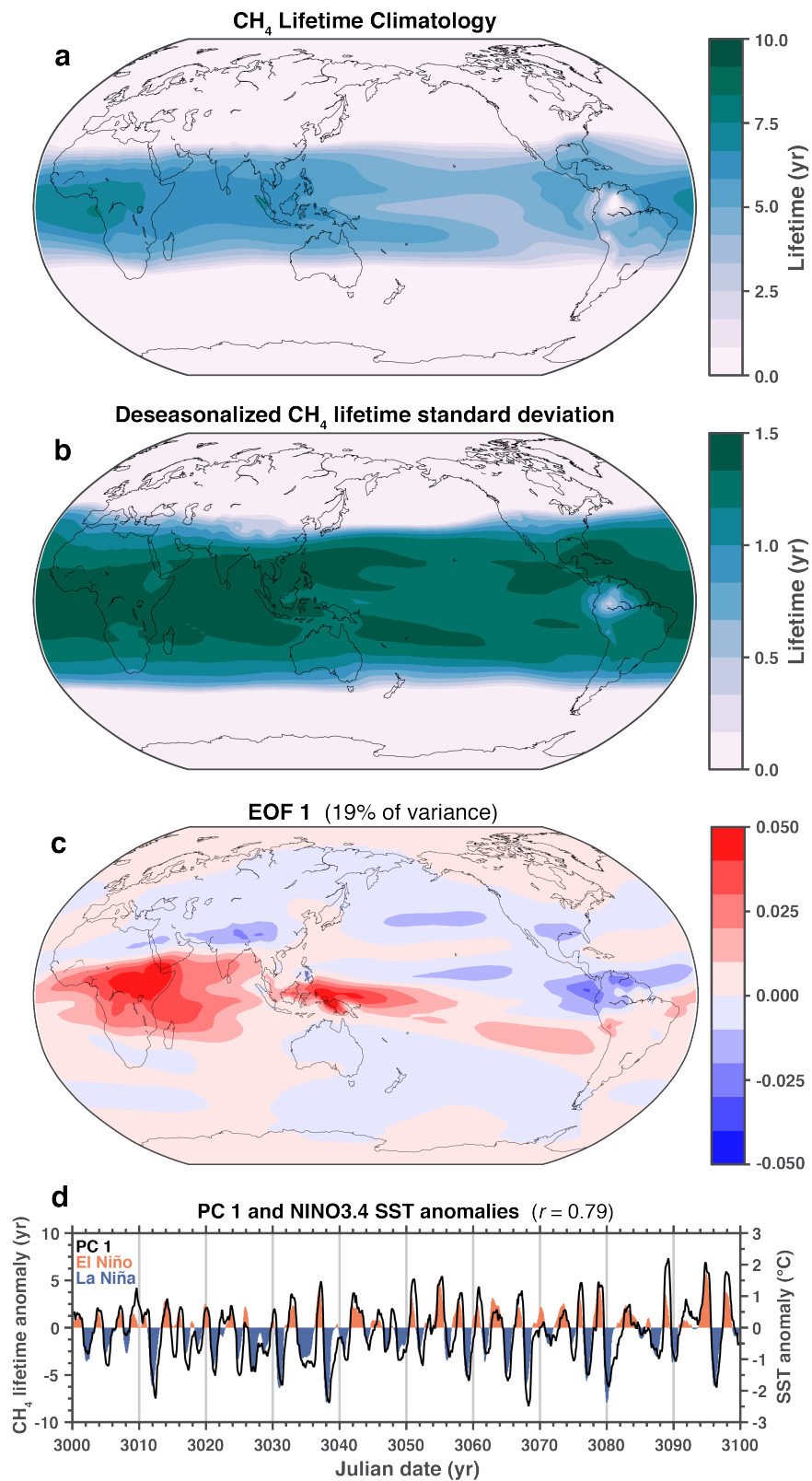


Fig. S10. Modes controlling the methane lifetime variability in a preindustrial control simulation. Same as main text Fig. 3 but for the methane loss frequency via reaction with OH. Computed as: $k(T) \times [\text{OH}]$ but the inverse is plotted (methane lifetime).

References

1. Holmes CD, Prather MJ, Søvde OA, Myhre G (2013) Future methane, hydroxyl, and their uncertainties: key climate and emission parameters for future predictions. *Atmospheric Chemistry and Physics* 13(1):285–302.